International Journal of Smart Grid (IJSmartGrid)
https://www.ijsmartgrid.org/ Online ISSN: 2602-439X
L.V. Dai and H.H.B. Nghia, Vol. 10, No. 1, March, 2026 Research Article

Advanced Control Technique for Optimizing Stability and Fault Recovery in Grid-Connected Solar Systems

Le Van Dai*‡, Huynh Hoang Bao Nghia*

*Electric Power System Research Group, Industrial University of Ho Chi Minh City, Ho Chi Minh City, Vietnam

(levandai@iuh.edu.vn, nghiabaohoanghuynh123@gmail.com)

‡Corresponding Author: Le Van Dai, Electric Power System Research Group, Industrial University of Ho Chi Minh City, Ho Chi Minh City, Vietnam.

Tel: +84 90167 2689, levandai@iuh.edu.vn

Received: 05.07.2025 Accepted:08.02.2026

Abstract- The primary purpose of this study is to enhance the operational stability and fault recovery capabilities of grid-connected photovoltaic (PV) systems, which frequently encounter challenges related to environmental variability and severe grid faults. To address these issues, the paper proposes an advanced maximum power point tracking (MPPT) controller utilizing an artificial neural network (ANN) trained with the Levenberg-Marquardt (LM) algorithm. The research procedure involves modelling a detailed grid-connected system comprising a DC-DC boost converter and a three-level neutral-point-clamped (NPC) inverter within the MATLAB/Simulink environment. The proposed control strategy is rigorously evaluated and compared with a conventional perturb-and-observe (P&O) method with dynamic step-size tuning under two distinct scenarios: normal operation with varying irradiance and severe three-phase-to-ground (LLLG) fault conditions. The main results demonstrate the superior performance of the proposed ANN-LM technique. Under normal conditions, the proposed method provides greater stability, with a total percentage overshoot of only 1.292%, which is significantly lower than the 1.496% observed with the conventional method. In the event of an LLLG fault, the proposed controller exhibits exceptional resilience, achieving a rapid voltage recovery time of 0.539 seconds compared to 0.713 seconds for the benchmark. Furthermore, the proposed technique improves power quality by limiting the inverter voltage total harmonic distortion (THD) to 122.37% during faults, whereas the conventional method reaches 147.31%. These findings confirm that the ANN-LM controller effectively optimizes energy extraction and ensures robust system operation in the face of grid disturbances.

Keywords: Grid-connected photovoltaic system, maximum power point tracking (MPPT), artificial neural network (ANN), Levenberg-Marquardt algorithm, fault recovery.

1. Introduction

In recent years, the field of power systems and renewable energy has made significant strides, focusing on advanced optimization and control techniques to reduce operating costs, mitigate emissions, and enhance grid reliability. A prominent research trend involves shifting towards multi-objective algorithms and intelligent control methods to address the increasing uncertainty of distributed resources. Renewable energy, particularly solar power, is

Cite this article as: L.V. Dai and H.H.B. Nghia, "Advanced Control Technique for Optimizing Stability and Fault Recovery in Grid-Connected Solar Systems" *International Journal of Smart Grid (ijSmartGrid)*, Vol. 10, No. 1, pp. 30–47, March, 2026.

increasingly pivotal in replacing fossil fuels due to its environmental benefits and abundant availability [1, 2]. In the context of the world facing increasingly serious challenges related to carbon emissions and climate change, the transition from fossil fuels to renewable energy sources, especially solar energy and photovoltaic (PV) systems, is an inevitable path. Studies show that integrating PV systems into energy and industrial systems has the potential to replace a significant portion of traditional electricity, thereby contributing to indirect CO_2 emission reductions at the system level through reduced fossil fuel demand [3]. Furthermore, energy and exergy analyses have demonstrated that harnessing PV energy in integrated structures not only improves overall energy efficiency but also significantly improves the environmental sustainability of modern energy systems [4, 5]. Furthermore, studies based on energy-exergy analysis and system structure optimization show that prioritizing clean, renewable energy sources, including solar energy, can significantly reduce the carbon emission intensity per unit of useful energy, thereby confirming the important role of PV systems in long-term carbon emission reduction strategies [6, 7].

Among renewable energy sources, PV systems are widely deployed globally, in both grid-connected and standalone configurations, serving diverse applications in energy production and the industrial sector [8, 9]. However, the energy conversion efficiency of PV systems is heavily influenced by environmental conditions such as shading, dust accumulation, temperature, and radiation intensity, which directly affect the determination of the maximum power point (MPP) [10]. Consequently, tracking and maintaining the MPP, also known as maximum power point tracking (MPPT), is a critical factor for optimal energy extraction. Although traditional algorithms, such as perturb and observe (P&O) and incremental conductance, are simple and easy to implement, they often struggle under rapidly changing weather conditions, leading to large oscillations and relatively low tracking accuracy [11].

Grid-connected PV systems typically comprise PV panels, DC-DC converters, DC-AC inverters, MPPT controllers, and grid synchronization controllers [12]. Beyond efficiency, stability is a paramount concern. When grid faults occur, such as voltage sags or severe three-phase-to-ground (LLLG) short circuits, the grid voltage can drop sharply within a short period, causing instability in the PV system and potentially forcing the inverter to disconnect [13, 14]. While the design of renewable energy systems has advanced, ensuring stability, robust control, and high fault ride-through performance remains a major challenge due to the complex nonlinear characteristics of these systems [11].

Enhancing the stability and reliability of power systems through intelligent optimization and control is a rapidly expanding research area. PV systems are generally categorized into two main types: grid-connected systems and standalone systems [15, 16]. To maximize performance, various optimization techniques have been investigated across different aspects of the smart grid [17]. For instance, in microgrid operation, the NSGA-II algorithm has proven effective in reducing costs and pollution by accounting for forecast errors in renewable sources [18]. Similarly, metaheuristic algorithms, such as genetic algorithms (GA) and particle swarm optimization (PSO), play a crucial role in optimizing energy storage systems for load flattening [19]. In the domain of protection and reliability, fuzzy logic methods have been applied to rapidly detect transformer failures. Improved bee algorithms have optimized the design of solar-wind hybrid systems to satisfy reliability constraints [20].

Furthermore, the artificial bee colony algorithm has demonstrated significant results in reducing losses in distribution grids, and Monte Carlo simulation, combined with multi-objective algorithms, has been utilized to address unit commitment problems under uncertainty. Regarding dynamic stability, optimal coordination between flexible AC transmission system devices and power system stabilizers has demonstrated superior oscillation-damping capabilities [21]. Additionally, studies on the aging process of insulation materials under contamination provide critical insights into component durability in outdoor environments [22]. These studies collectively aim to develop optimal control strategies that adapt to strong fluctuations in load and renewable sources while ensuring cost-effectiveness, stability, and reliability. This forms the basis for discussing the main objective of this paper.

Specific improvements to MPPT algorithms have also been extensively explored. In study [23], an enhancement to the traditional P&O algorithm was proposed by incorporating current change information to address the “drift” phenomenon caused by sudden irradiance changes. Similarly, a study [24] modified the incremental conductance algorithm to mitigate incorrect responses under rapidly changing conditions, increasing tracking speed by approximately 20-30%. To address partial shading, study [24] proposed a hybrid of the simulated annealing algorithm and P&O, effectively preventing the system from being trapped in local maxima. Furthermore, the slime mold golden sine algorithm was presented in [25] to offer superior convergence speed compared to PSO and other heuristic methods. Another strategy involving variable-step-size P&O using GA was discussed in [21], which adjusts the step size based on proximity to the MPP to balance speed and oscillation.

Despite these advancements, traditional and heuristic methods can still struggle with the nonlinear complexities of PV systems under severe disturbances. Consequently, machine learning techniques, particularly artificial neural networks (ANNs) [26], have emerged as powerful tools for MPPT. ANNs can model the nonlinear relationship between inputs, such as voltage, current, temperature, and output power, without requiring prior mathematical assumptions. In this study, an ANN-based MPPT controller is designed using a dataset of historical voltage and current values to estimate the optimal duty cycle for the DC-DC converter. Unlike standard training algorithms, this study employs the Levenberg-Marquardt (LM) algorithm, an efficient quasi-Newton optimization technique, to train the network, enabling rapid convergence with minimal error.

The ANN trained with the LM algorithm not only improves power prediction accuracy but also ensures high stability and adaptability under rapidly changing weather

conditions. The primary objective of this research is to design an intelligent MPPT controller that quickly locates the GMPP while minimizing power fluctuations. The proposed method is validated through simulations involving irradiance changes and, crucially, under an LLLG fault scenario, utilizing fault analysis methodologies consistent with previous research [27]. The results demonstrate that the proposed controller significantly reduces harmonic distortion, enhances the quality of the DC bus voltage, and ensures rapid system recovery.

This study contributes to control theory by demonstrating an advanced control framework that enhances the stability and fault tolerance of photovoltaic systems under grid failures. The research provides system-level insights into the dynamic interaction between photovoltaic systems and the grid during faults, supporting the reliable integration of large-scale photovoltaic systems in compliance with grid regulations. In summary, the main contributions of this research are presented as follows:

- This paper introduces a novel approach for the MPPT controller utilizing an ANN trained with the LM algorithm. This method enables precise system identification and dynamic control of parameters, optimizing energy extraction from PV panels under varying irradiation and temperature conditions.

- The system is simulated under an LLLG fault scenario, demonstrating that the proposed controller exhibits high resilience. The system recovers quickly and resumes stable operation after the fault, showcasing the robustness and adaptability of the controller under real-world conditions.

- The proposed method significantly reduces harmonic distortion and enhances the quality of the DC bus voltage. This improvement minimizes performance losses caused by harmonic interference and optimizes the DC-AC energy conversion process.

The primary objective of this study is to develop and validate an intelligent MPPT strategy for grid-connected PV systems, ensuring rapid global MPPT, high operational stability, and robust fault tolerance under severe grid disturbances. Specifically, this study aims to design an MPPT controller based on an ANN trained with the LM algorithm to accurately estimate the optimal duty cycle of a DC-DC converter under rapidly changing radiation and temperature conditions. In addition to improving steady-state power extraction capabilities, the proposed controller is evaluated under severe LLLG conditions to assess its robustness, dynamic recovery performance, and impact on DC bus voltage quality and harmonic distortion. Through comprehensive simulation analysis, this study seeks to demonstrate that the proposed ANN-LM-based MPPT method offers superior performance compared to conventional MPPT techniques in terms of tracking accuracy, system stability, and grid fault tolerance.

One of the main advantages of this study lies in the integration of an ANN-based MPPT controller with the LM training algorithm, enabling rapid convergence and high prediction accuracy without the need for a specific mathematical model of the PV system. This data-driven approach effectively captures the nonlinear behavior of PV characteristics under varying environmental conditions. Another key strength is the comprehensive evaluation of system performance under both normal operating conditions and severe grid disturbances. By considering the LLLG fault scenario, this study goes beyond conventional MPPT performance evaluation and demonstrates the robustness and fault tolerance of the proposed controller. Furthermore, the reduction of harmonic distortion and improvement of DC bus voltage quality highlight the practical benefits of the proposed method in enhancing overall energy conversion efficiency and grid compatibility. Despite these advantages, the proposed method still has some limitations. The performance of ANN-based MPPT controllers is highly dependent on the quality and representativeness of the training dataset. Insufficient or skewed training data can reduce tracking accuracy under unknown operating conditions. Furthermore, the computational complexity of training ANNs using LM algorithms can make real-time deployment on inexpensive embedded platforms challenging, especially in large-scale optoelectronic systems. Moreover, this research is primarily validated through simulation. While the results show promising performance, experimental validation on a hardware test system is necessary to fully assess real-world implementation issues such as sensor noise, parameter uncertainty, and communication latency. These aspects will be addressed in subsequent studies.

Following this introduction, the paper is organized into several sections. Section 2 details the grid-connected solar energy conversion system. Section 3 discusses the proposed control solutions. Section 4 presents the simulation results under both normal and fault conditions. Finally, the conclusion summarizes the research's key findings.

2. Grid-Connected PV Solar Energy Conversion System

Fig. 1 shows the configuration of the grid-connected PV control system. The PV array is rated at 219.961 W under standard test conditions, 1000 W/m^2 irradiance, and 25°C cell temperature. It is interfaced with a dedicated DC-DC boost converter. The converter is controlled by an ANN-based MPPT algorithm to regulate the PV terminal voltage and ensure maximum power extraction. The boost converter output is connected to a common DC-link with a nominal voltage of 1000 V.

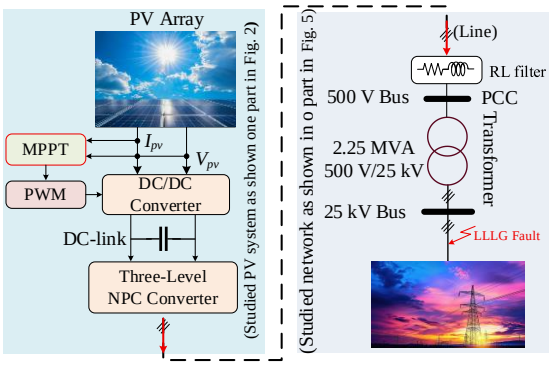

Fig. 1. Grid-connected solar power system.

The energy is then converted to three-phase AC via a three-level neutral point clamped (NPC) inverter, producing an AC voltage of approximately 500 V. A DC voltage link controller controls the inverter to maintain a DC voltage of 1000 V despite variations in input power from the PV arrays. Additionally, the system is equipped with a reactive power controller, allowing the inverter to either generate or absorb reactive power up to ±1 MVAr. To connect to the grid, the system uses a three-phase transformer with a power rating of 2.25 MVA and a voltage rating of 500 V/25 kV. The grid-side model includes a 25 kV distribution line and a 120 kV transmission grid.

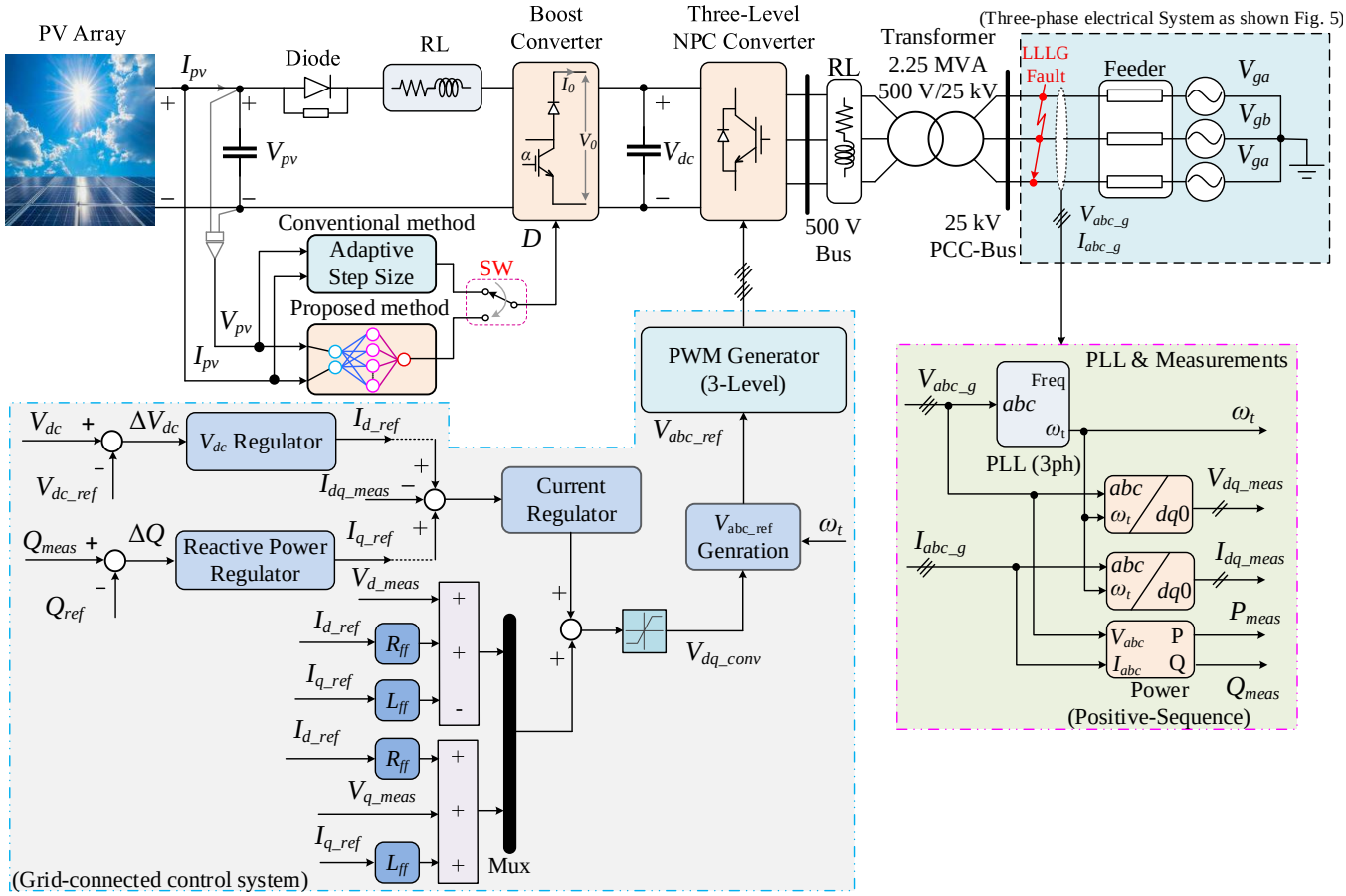

Fig. 2. The control method of the studied grid-connected solar energy.

Fig. 2 illustrates the connection between the PV array and the grid, which involves key components such as the solar panel, boost converter, DC link [31], three-phase inverter, RL filter, step-up transformer, and the electrical grid. In this system, the grid-connected PV uses a three-level NPC inverter and a sophisticated control structure that integrates artificial intelligence. The input energy from the PV array is processed through a diode and an RL filter before entering the boost converter, which steps up the V_{pv} to the DC link voltage V_{dc}. The MPPT control is executed in parallel by two algorithms: the traditional P&O algorithm, which uses an adaptable step size, and the proposed LM-based algorithm. This enables the system to switch flexibly between these two algorithms depending on the actual operating conditions.

The MPPT signal is then used to control the boost converter's duty cycle (D). The DC voltage from the boost converter is fed to the three-level NPC inverter, where it is converted to a three-phase AC voltage and filtered by the RL circuit. The signal then passes through the transformer and is connected to the grid via the distribution line. In terms of control, the system employs a double closed-loop control strategy, comprising current control and reactive power control. The measured outputs from the grid, V_{abc_g} and I_{abc_g}, are fed into a phase-locked loop (PLL) block to extract synchronized components such as frequency, real power P_{mean}, and reactive power Q_{mean}, as well as voltage and current components in the dq frame.

The reactive power regulator block handles the error between the actual and reference reactive power Q_{ref}, adjusting the reference current I_{q_ref}. Similarly, the V_{dc} regulator block controls the reference current I_{d_ref} to maintain a stable DC voltage. All control signals, I_{d_ref} and I_{q_ref}, are compared with the actual currents I_{d_mean} and I_{q_mean}, and the error is sent to the current regulator block to compute the control voltage V_{dq_conv}, which generates the three-phase reference voltage V_{abc_ref} for the three-level PWM controller.

2.1. Photovoltaic Array Model

The goal of equivalent circuit models [29] is to represent the overall I-V characteristic of a PV cell, module, or array as a continuous mathematical relationship involving key electrical variables. A PV array is formed by connecting multiple PV modules in series to achieve the desired voltage and in parallel to provide the required current. This

configuration allows the system to efficiently meet specific power requirements. The equivalent circuit model representing a PV module arranged in n_p parallel and n_s series connections is illustrated in Fig. 3 [28].

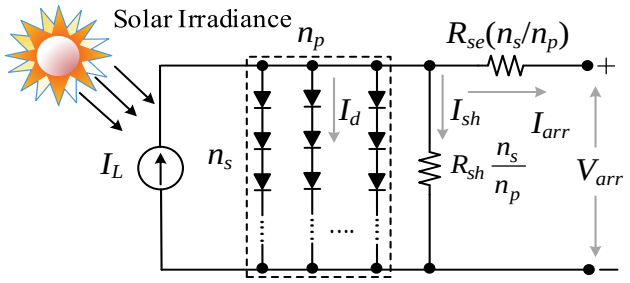

Fig. 3. Electrical equivalent model of a photovoltaic array.

To mathematically describe the equivalent circuit of a PV cell, Kirchhoff's current law is applied, leading to the following expression for the output current [29].

$$I_{arr} = I_L - I_d - I_{sh} \tag{1}$$

where I_L is the photocurrent generated by sunlight, I_d is the loss diode current, and I_{sh} is the photocurrent generated by sunlight. The diode current I_d in a single-diode PV model follows the Shockley equation for an ideal diode [30].

$$I_d = I_s\left(\exp\left(\frac{(V_{arr} + R_{se}I_{arr})q}{n(kT_c/q)}\right) - 1\right) \tag{2}$$

where I_s is the reverse saturation current of the diode, q is the electron charge 1.6×10^{-19} C, n is the diode ideality factor typically between 1 and 2, R_{se} is the internal series resistance, V_{arr} is the terminal voltage of the PV cell, k is the Boltzmann's constant 1.38×10^{-23} J/K, and T_c is the is the cell's junction temperature in Kelvin. Meanwhile, the shunt current I_{sh}, caused by leakage through the shunt resistance R_{sh}, is given as follows.

$$I_{sh} = \frac{(V_{arr} + R_{se}I_{arr})q}{R_{sh}} \tag{3}$$

Combining these relationships, the final expression for the output current of the single-diode PV model as follows.

$$I_{arr} = I_L - I_s A - \frac{(V_{arr} + R_{se}I_{arr})q}{R_{sh}} \tag{4}$$

in with $A = \exp\left(\frac{(V_{arr} + R_{se}I_{arr})q}{n(kT_c/q)}\right) - 1$.

This comprehensive formulation captures both the diode's nonlinear characteristics and the effects of resistive losses within the PV cell. As illustrated in Fig. 3, the equivalent circuit of a PV array consists of multiple PV cells arranged with n_s cells in series and n_p strings in parallel. The overall output current of the array can be expressed using the following relation.

$$I_{arr} = n_p I_L - n_p I_s B - \left(\frac{(V_{arr} + R_{se}(n_s/n_p)I_{arr})q}{R_{sh}(n_s/n_p)}\right) \tag{5}$$

where $B = \exp\left(\frac{(V_{arr} + R_{se}(n_s/n_p)I_{arr})q}{n_s n(kT_c/q)}\right) - 1$, in which V_{arr} is the total voltage of the array, and I_{arr} is the total output current. Therefore, the reverse saturation I_s is the diode current, n is the diode coefficient.

The simulation and demonstration are based on a Solarex PV module, Canadian Solar Inc. CS5P-220M [31], consisting of 66 polycrystalline cells connected in series Table 1. The I-V and P-V characteristics of the P-V array are illustrated in Figs. 4a and 4b.

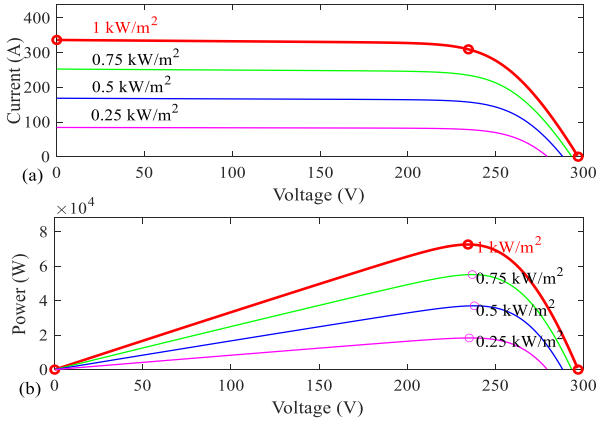

Fig. 4. Specifications of a PV array; (a) the I-V characteristic and (b) the P-V characteristic.

Table 1. The unique electrical properties of a single module

PV panel parameters	Symbols	Values
Maximum power	P_{max}	219.961W
Cells per module	n_{arr}	96
Open circuit voltage	V_{oc}	59.40 V
Short-circuit current	I_{sc}	5.10 A
Voltage at MPP	V_{mp}	46.90 V
Current at MPP	I_{mp}	4.690 A
Temperature coefficient of V_{oc}	%/deg.C	-0.374
Temperature coefficient of I_{sc}	%/deg.C	0.089
Cell-temperature	t_c	25 ºC

2.2. DC/DC Converter Model

One of the essential components of this system is the DC/DC boost converter, which increases the voltage from the PV array to the level required for conversion to AC via the inverter and grid integration. This converter plays a vital role in boosting the DC voltage from the PV array to the optimum level for efficient use in conversion to AC and grid integration, as shown in Fig. 2. The DC/DC boost converter is controlled by the duty cycle, with the output voltage V_0 and current I_0 related to the input voltage and current as follows:

$$\begin{cases} V_0 = \dfrac{V_{pv}}{1-\alpha} \\ I_0 = I_{pv}(1-\alpha) \end{cases} \quad (6)$$

where α is obtained as the output of the MPPT control system.

2.3. RL Filter

The RL filter is incorporated into the inverter to enhance the load current and minimize switching losses in the power components. The inductance value is determined by the current ripple, which typically ranges from 15% to 25% of the rated current. To calculate the appropriate inductance, the maximum current ripple can be calculated as follows.

$$\Delta i = \frac{1}{8}\frac{V_{dc}}{L_f f_{sw}} \quad (7)$$

where V_{dc} is the DC voltage, L_f is the filter inductance, and f_{sw} is the inverter switching frequency. The inductance value L_f in this system is typically set so that the current ripple does not exceed 20% of the rated current. The RL filter plays a crucial role in minimizing inverter-induced harmonic distortion, improving current quality, and mitigating negative impacts on the system's electronic devices.

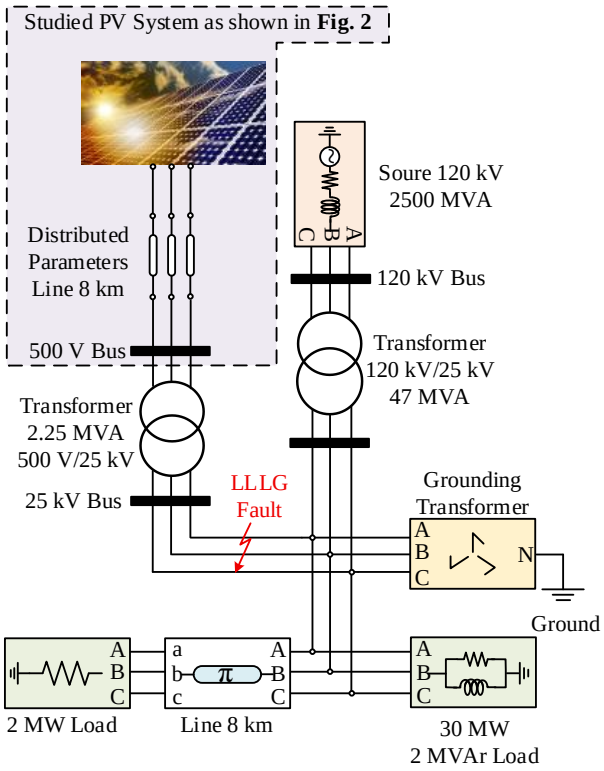

Fig. 5. The model of a three-phase electrical system.

2.4. Model of Different Grid Elements

This model simulates a three-phase electrical system, including key components such as a three-phase transformer, three-phase power source, transmission lines, and RLC loads in Fig. 5. The transformer has an input voltage of 120 kV and an output voltage of 25 kV, with a power rating of 47 MVA, which adjusts the voltage between different levels of the system. The three-phase power source provides energy to the system, with a voltage of 120 kV and a power rating of 2500 MVA. The model also features a grounding transformer to safeguard the system in the event of faults, ensuring the safety of both personnel and equipment.

The transmission lines, with lengths of 8 km, 2 km, and 6 km, model the distributed parameters such as resistance and reactance, which affect the power transmission and system efficiency. The three-phase parallel RLC loads, rated at 30 MW and 2 MW, simulate energy-consuming devices, enabling analysis of the load's impact on system stability. Voltage and current measurements at key points enable monitoring and ensure proper system operation, allowing early fault detection and performance optimization. This model helps analyze the stability and efficiency of the three-phase electrical system when the system operates under normal conditions and when an LLLG occurs.

3. Proposed Control Solution for Maximum Power Point Tracking

3.1. Dynamic Step Size Tuning Solution

This improved P&O MPPT algorithm adjusts the dynamic step-size tuning during MPP tracking. The process begins by measuring the voltage and current of the PV array at a time. The PV power at this time is calculated as follows.

$$P_{pv}(t) = V_{pv}(t) I_{pv}(t) \quad (8)$$

Next, the algorithm calculates the change in power and voltage between time (t) and ($t-1$), as follows.

$$\Delta P_{pv}(t) = V_{pv}(t) I_{pv}(t-1) \quad (9)$$

$$\Delta V_{pv}(t) = V_{pv}(t) V_{pv}(t-1) \quad (10)$$

This calculation of the changes helps the system understand the trend in power and voltage, allowing it to decide the direction of the next adjustment. Once the changes in power and voltage are computed, the algorithm calculates the step-size adjustment as follows.

$$\Delta D = N(\text{abs}(\Delta P_{pv} + \Delta V_{pv} \Delta I_{pv})) \quad (11)$$

where N is a scaling factor that helps adjust the step size appropriately. When there is a significant change in power, the step size will be large to help track the MPP quickly. Conversely, when power changes are small, the step size decreases to avoid oscillations around the MPP.

The algorithm continues by checking three key conditions. If $\Delta P_{pv}(t) = 0$, indicating no change in power, the algorithm will not change the step size and will continue tracking the current state. If $\Delta P_{pv}(t) > 0$, meaning power is increasing, the algorithm will increase the step size to track the MPP faster. If $\Delta P_{pv}(t) < 0$, meaning power is decreasing, the algorithm will reduce the step size and reverse direction to move closer to the MPP.

The step-size adjustment is crucial for improving the efficiency of the MPPT algorithm, enabling the system to dynamically adapt to changing environmental conditions, minimize oscillations around the MPP, and thereby ensure faster convergence.

$$D(t+1) = D(t) \pm \Delta D \tag{12}$$

where $D(t)$ is the duty cycle at time, $D(t + 1)$ is the duty cycle at the next time step $(t + 1)$, and $\pm\Delta D$ means the step size can either be added or subtracted, depending on the change in power ΔP between the two time steps. Finally, after each adjustment, the values of $D(t)$, $V_{pv}(t)$, $I_{pv}(t)$, and $P_{pv}(t)$ are stored and used in the next iterations, allowing the system to continue tracking the MPP stably. This method helps reduce oscillations and improve MPPT accuracy, especially under rapidly changing environmental conditions such as solar irradiance and temperature. Fig. 6 illustrates the flowchart of the proposed P&O MPPT approach with an adaptable step size.

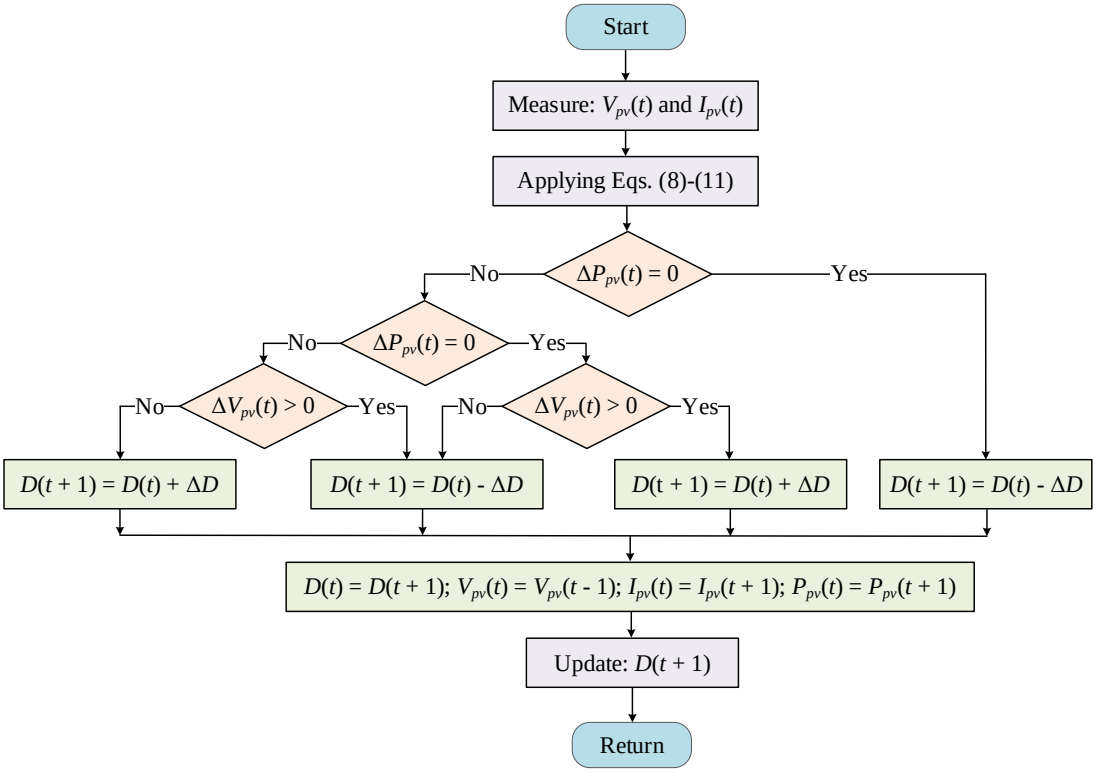

Fig. 6. Flowchart of the P&O MPPT algorithm using the dynamic step size tuning solution.

3.2. Artificial Neural Network Solution

Fig. 7 presents a neural network architecture with two layers, each incorporating bias (b) and weight (W) elements. The inputs are first combined with the bias, then passed through an activation function, represented by the curved line in Layer 10 and the straight line in Layer 2. This design allows the input data, which includes two signals as voltage and current, to undergo nonlinear transformations. As a result, the network is capable of learning complex patterns and relationships between the input data and the output signal, which corresponds to the D [32].

LM is a widely used optimization algorithm for training an ANN. It is especially effective at addressing nonlinear regression issues and determining optimal weights to minimize the discrepancy between predicted and target outputs. The LM method combines the Gauss-Newton and steepest descent approaches, iteratively adjusting the weights to reduce the error, typically quantified by the mean squared error (MSE).

The deployment of ANN optimized via the LM algorithm has emerged as a cornerstone for enhancing the efficacy of PV systems. This computational approach is not merely an engineering preference but a strategic necessity to minimize the carbon footprint of energy-intensive processes by maximizing renewable penetration. The architectural workflow begins with the acquisition of stochastic physical signals: PV voltage V_{pv} and current I_{pv}. To ensure numerical stability and prevent gradient saturation, a common pitfall, deep learning input signals are subjected to a normalization process within the input block. This maps the physical domain into a closed interval using the min-max transform:

$$x_{\text{norm}} = 2\frac{x - x_{\min}}{x_{\max} - x_{\min}} - 1 \tag{13}$$

where $x_{\min}$ and $x_{\max}$ are the minimum and maximum values of

the training dataset, respectively, and x is the actual value V_{pv} or I_{pv}. Upon entering Layer 1, the system uses a tapped-delay line. From my experience, this is critical for PV applications as it provides the network with temporal awareness, allowing it to remember previous irradiance states. The mathematical core of this layer consists of 15 parallel neurons. Each neuron i computes a weighted sum of the inputs based on the input weight matrix IW{1,1}, defined as:

$$z_i = \sum_{j=1}^{R} w_{i,j} p_j \tag{14}$$

This weighted input is then biased by b_i to adjust the decision threshold as follows.

$$n_i = z_i + b_i \tag{15}$$

To capture the highly nonlinear characteristics of semiconductor devices under varying environmental conditions, the Hyperbolic Tangent Sigmoid activation function is employed and can be defined as follows.

$$a_i = \text{tansig}(n_i) = \frac{e^{n_i} - e^{-n_i}}{e^{n_i} + e^{-n_i}} \tag{16}$$

The hallmark of this specific implementation is the LM training protocol. Unlike standard gradient descent, the LM algorithm provides a robust bridge between the Gauss-Newton method and the steepest descent. It updates the weight vector w by approximating the Hessian matrix and can be calculated as follows.

$$w_{k+1} = w_k - [J^T J + \mu I]^{-1} J^T e \tag{17}$$

where J is the Jacobian matrix and μ is the damping factor. This ensures rapid convergence even in complex search spaces, which is vital for real-time MPPT control. The latent features processed in Layer 1 are then aggregated in the output Layer 2 through a linear transfer function, denoted as purelin, and computed as follows.

$$a\{2\} = \text{IW}\{2,1\} \times a\{1\} + b\{2\} \tag{18}$$

Finally, the process output block performs de-normalization to translate the network's abstract output into a tangible PWM signal, denoted as D, and determined as follows.

$$D = \frac{(a\{2\}+1)(D_{\max} - D_{\min})}{2} + D_{\min} \tag{19}$$

By integrating ANN-LM control into PV systems to maximize power output from PV arrays using precise nonlinear control, a faster, more stable transition towards high-power renewable energy integration is facilitated. Ultimately, this framework ensures dynamic stability and enhances system efficiency, maintaining optimal operating points even under rapidly changing atmospheric conditions, thereby guaranteeing a robust and sustainable energy architecture.

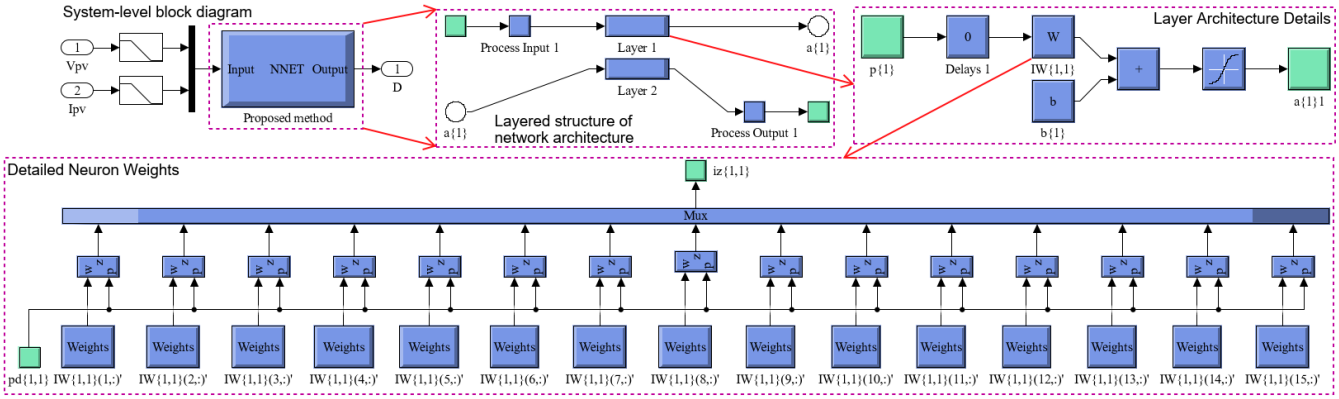

Fig. 7. Feedforward neural network architecture.

The LM algorithm adjusts the step size based on the curvature of the error surface, using a damping parameter to balance local and global search directions. This approach ensures fast convergence and stability while avoiding local minima. LM is effective in approximating the Hessian matrix without requiring direct computation, making it suitable for large networks. The algorithm is also resistant to local minima and automatically adjusts during training. It is widely used in machine learning due to its fast convergence and efficient handling of complex error surfaces [33].

Based on the regression plots in Fig. 8, we observe high accuracy in the artificial neural network training and testing model using the LM algorithm. Specifically, during the Training phase, the training correlation coefficient (R) value is 0.93129; see Fig. 8a. The relationship between the output and target fits well with the dotted line (Y = T). The training R value of 0.93129 indicates that the model has been trained effectively, with relatively small errors between the actual data and the predicted values. In the validation phase, the validation R value of 0.93024, shown in Fig. 8b, indicates

that the model generalizes well when applied to the validation data. The output is still close to the target value, although there is a slight decrease in accuracy compared to the training phase. During the test phase, the test *R* value was 0.93142. As shown in Fig. 8c, the model performs excellently on the test data, achieving a test *R* value of 0.93142. This demonstrates that the model can accurately predict not only on training and validation data but also on completely new data. The overall *R* value of 0.93115; Fig. 8d combines the training, validation, and test phases, showing an overall regression *R* value of 0.93115.

This indicates that the model maintains accurate and stable prediction performance across all datasets. The high regression values across all phases indicate that the LM algorithm has effectively trained the ANN, with minimal error and strong generalization across training, validation, and test data.

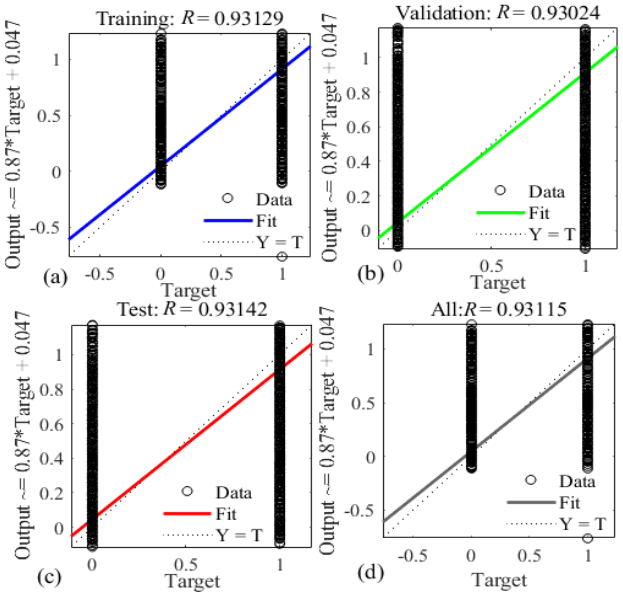

Fig. 8. Regression plot of the LM algorithm with the different correlation coefficient (*R*): (a) the training *R* value of 0.93129, (b) the validation *R* value of 0.93024, (c) the test *R* value of 0.93142, and (d) the overall *R* value of 0.93115.

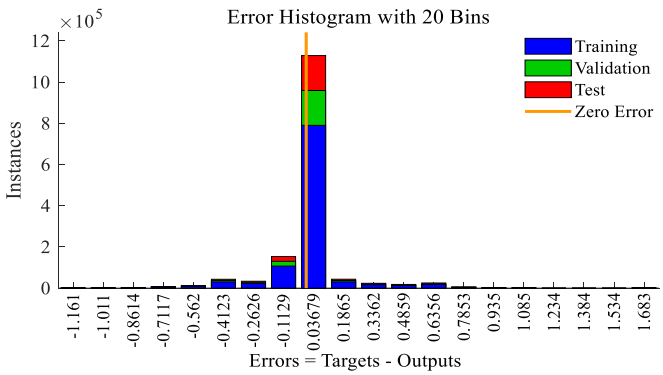

Fig. 9. Error histogram plot of the LM algorithm.

The error histogram in Fig. 9 shows the results obtained with the artificial neural network using the LM algorithm. This histogram consists of a total of 20 bins, with errors ranging from -1.161 to 1.683. The data is distributed across these bins, with errors mainly concentrated in the range from -1.161 to 1.683. Notably, the bar representing 0% error indicates that some samples have zero errors, demonstrating that the model has learned accurately and made almost perfect predictions. These results show that the ANN has effectively optimized the MPPT with minimal error, achieving accurate convergence during the training, test, and validation phases.

Figs. 10a -10c and Fig. 11 illustrate both the training and performance evaluation phases of the artificial neural network used to process the selected dataset. The validation checks for the training dataset, as well as the gradient and momentum (mu) parameters at 1000th epochs, are shown in Fig. 9. The simulation results indicate that at the 1000th epoch, the gradient value is 0.031757, suggesting minimal variance from the training data and a small loss function. These results imply that the cumulative error is primarily due to the decision to generate zero outputs and the average value for each input vector. The effectiveness of the LM algorithm for MPPT is evident from the very low gradient values and the validation tests on the training dataset.

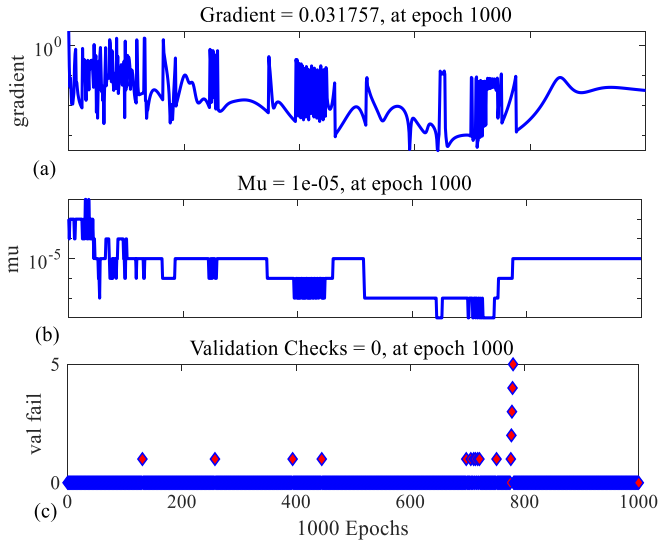

Fig. 10. Training test plot of the LM algorithm; (a) the gradient, (b) the mu, and (c) the valfail.

Fig. 11 shows the MSE for the samples in the training dataset across different epochs, indicating an optimal training outcome at the 1000th epoch. As a result, the dataset achieves the highest validation performance after 1000th epochs. Based on the simulation results, the validation performance of 0.030737 at the 1000th epoch is the best. The MPPT estimation using the LM method achieved nearly zero validation performance, indicating a very low error rate.

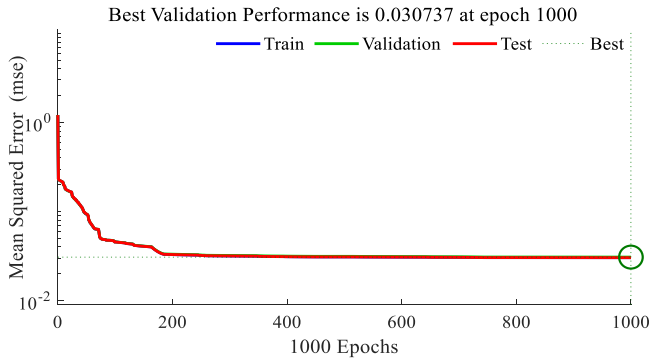

Fig. 11. Performance plot of the LM algorithm.

4. Results and Simulation

A control system for connecting a PV array to the grid has been developed and comprehensively simulated in MATLAB/Simulink. A comparative analysis is performed to evaluate the performance and efficiency of the proposed control strategy. Specifically, the study focuses on assessing the robustness and dynamic response of the controller under two distinct conditions: normal operation and during an LLLG fault. The proposed control system exhibits strong stability and reliable performance in both scenarios, demonstrating its resilience and adaptability to disturbances. The simulation model is constructed and illustrated in Fig. 2, with the PV panel parameters provided in Table 1 and the system parameters presented in Appendix 1.

In the simulation of the system control using the ANN controller trained with the LM algorithm, the following parameters are set: the DC voltage supplied to the rectifier is V_{dc} = 1000 V throughout the simulation, the switching frequency is $T_s = 2.5\times10^{-5}$ seconds, and the simulation time is t = 2.5 seconds in without fault, and t = 1.5 seconds in with fault. The simulation, conducted in MATLAB/Simulink, aims to evaluate the performance of the proposed MPPT control method compared to the conventional method that incorporates a dynamic step-size tuning solution.

4.1. Case Study 1

Considering Normal Operating Conditions: The initial analysis of the grid for all parameters is carried out without any faults in the distribution network, with irradiance set as shown in Fig. 12. Based on Figs. 13a - 13c, both MPPT algorithms, the conventional method and the proposed method, maintain stable voltage and current for the PV arrays, with the proposed method demonstrating better stability throughout the simulation. Specifically, while the voltage of PV arrays remains stable at high levels in both methods, the proposed method maintains smoother power and achieves optimal values more quickly compared to the conventional method.

Fig. 14 illustrates the DC-link voltage under the control of two MPPT algorithms: the proposed method and the conventional method. The DC-link voltage is controlled to maintain stability, as indicated by the red reference voltage line. From the figure, it can be observed that while the conventional method causes significant fluctuations in the DC-link voltage, the proposed method maintains a more stable voltage with fewer variations.

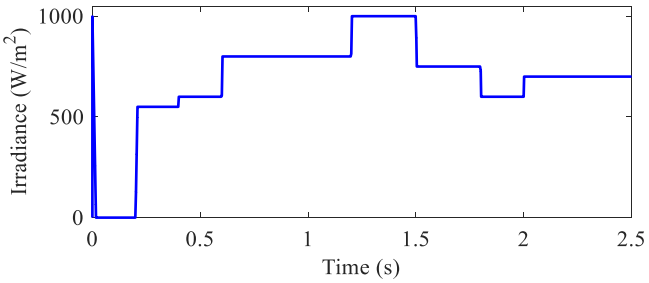

Fig. 12. The solar irradiance pattern applied to PV arrays.

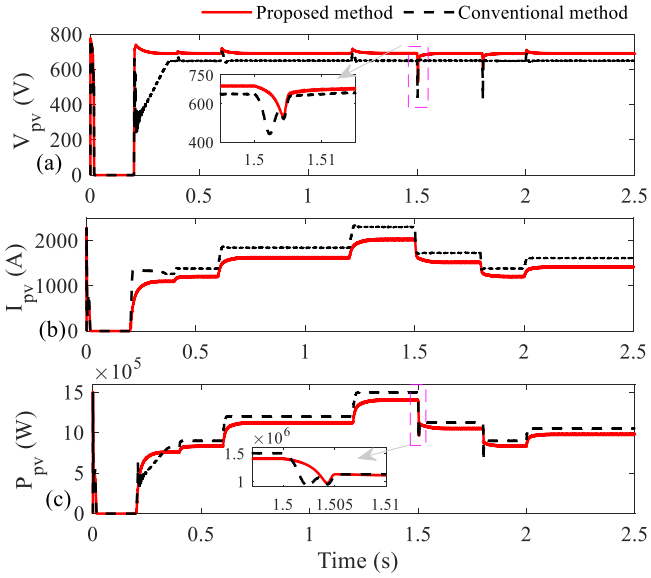

Fig. 13. The PV panel parameters: (a) the voltage, (b) the current, and (c) the active power.

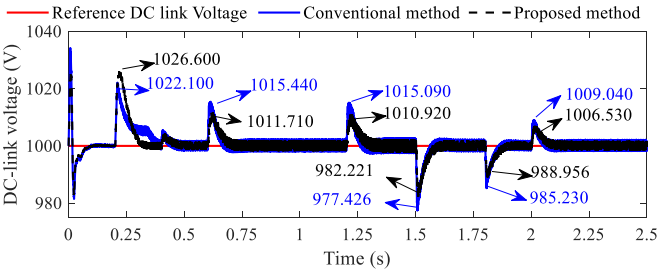

Fig. 14. Dynamic performance of the DC-link voltage under normal operating conditions.

The current of the PV arrays increases similarly in both methods, but the proposed method experiences fewer fluctuations. Table 2 summarizes the voltage, current, and power values for the two panels, showing that from 0.2 to 0.4 seconds, the power of both PV arrays increases, but the conventional method produces lower power than the proposed method. Meanwhile, the proposed method

maintains more stable power and is less affected by changes in irradiance conditions.

Specifically, with the conventional method, the DC-link voltage fluctuates strongly around the reference value, as shown in Table 3, and both methods exhibit voltage overshoot. The percentage overshoot total (%POT) indicates that the proposed method is more effective at maintaining a stable DC-link voltage than the conventional method. Specifically, the conventional method yields a total % POT of 1.496%, while the proposed method yields 1.292%. This indicates that the proposed method causes less fluctuation and overshoot, helping to maintain better voltage stability throughout the operation.

Figs. 15a and 15b show the voltage at the PCC bus with a constant, where the peak voltage per phase is 2×10^4 V. Regardless of variations in the injected power from the combined system, the PCC bus voltage for both the conventional method and proposed methods remains stable. This demonstrates the ability of both methods to maintain voltage stability despite fluctuations in irradiance or changes in input power conditions.

Table 2. Summary of PV array values by the conventional and the proposed methods in case study 1

Time (seconds)	PV array values					
	Conventional method			Proposed method		
	V_{pv} (V)	I_{pv} (A)	$P_{pv}\times10^5$ (W)	V_{pv} (V)	I_{pv} (A)	$P_{pv}\times10^5$ (W)
0 - 0.2	0	0	0	0	0	0
0.2 - 0.4	646.017	1333.550	8.23825	689.519	1086.800	7.53377
0.4 - 0.6	645.563	1377.380	8.99997	689.959	1194.290	8.26264
0.6 - 1.2	647.657	1873.300	12.02330	690.494	1611.230	11.16610
1.2 - 1.5	647.860	2317.430	15.01660	691.413	2013.750	13.95530
1.5 - 1.8	653.187	1721.640	11.26930	690.257	1507.730	10.44850
1.8 - 2.0	645.653	1376.910	9.00257	689.373	1194.610	8.27390
2.0 - 2.5	647.220	1607.700	10.51800	690.145	1404.500	9.87954

Table 3. Overshoot and stability of DC-link voltage for the conventional and the proposed methods

Time (seconds)	Stidied values				
	References	V_{dc} (V)		POT (%)	
	V_{dc} (V)	Conventional method	Proposed method	Conventional method	Proposed method
0.2	1000	1022.100	1026.600	2.162	2.591
0.6		1015.440	1011.710	1.520	1.157
1.2		1015.090	1010.920	1.486	1.080
1.5		977.426	982.221	2.309	1.810
1.8		985.230	988.956	1.499	1.116
2.0		1009.040	1006.530	0.895	0.648
Total				1.496	1.292

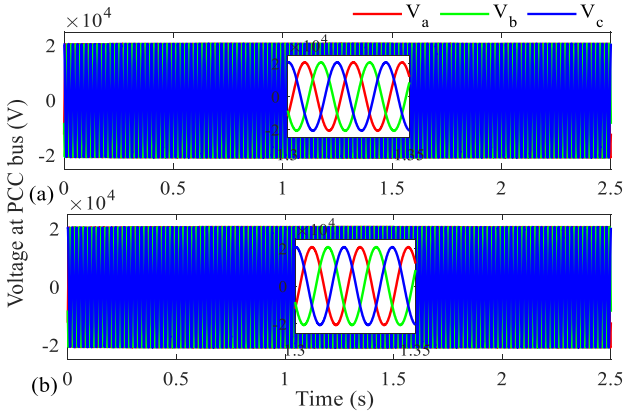

Fig. 15. Dynamic performance of the voltage at the PCC bus under normal operating conditions: (a) proposed method and (b) the conventional method.

The current data for the PCC bus is distributed across three phases, as shown in Figs. 16 and 16b. When irradiance conditions change, slight variations in the current of each phase can be observed, but the voltage remains stable and undistorted, indicating the effectiveness of both the conventional and proposed methods in maintaining voltage quality under external changes. This shows that both methods are effective in maintaining system stability, especially when irradiance and injected power fluctuate.

Based on Figs. 17 and 18, it can be observed that both the active and reactive power of the system under the control of the conventional and proposed method algorithms remain stable, with the proposed method showing superior stability. Specifically, the active power of the system remains stable at 2.5 MW, with the proposed method more effective at maintaining this level without significant fluctuations, whereas the conventional method shows slight variations in active power. Regarding reactive power, the system maintains 0.911 MVAr, indicating a relatively high level, while the power factor remains close to 1, ensuring high operational efficiency and minimizing energy losses. Both algorithms maintain stable reactive power at 0.911 MVAr, but the proposed method better preserves the stability of both active and reactive power, particularly under changing irradiance conditions.

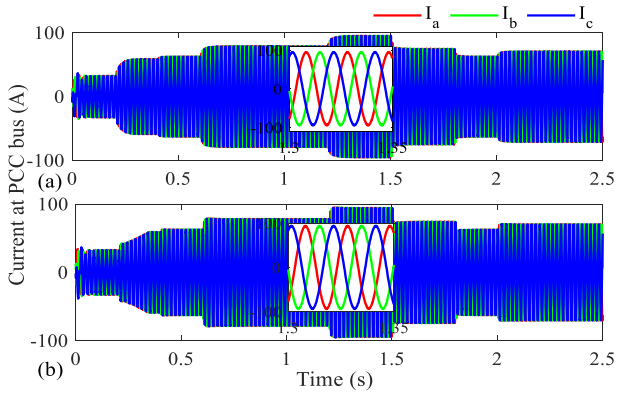

Fig. 16. Dynamic performance of the current at the PCC bus under normal operating conditions: (a) proposed method and (b) the conventional method.

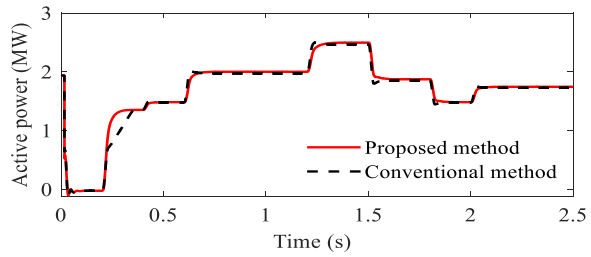

Fig. 17. The active power under normal operating conditions.

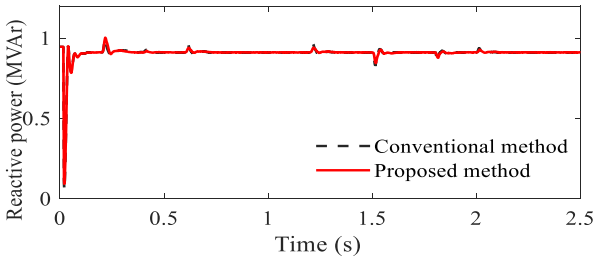

Fig. 18. The reactive power under normal operating conditions.

Based on the analysis of Figs. 19a and 19b show a clear distinction between the two MPPT control methods, the proposed method, and the conventional method, in terms of voltage waveforms, phase current, and harmonic distortion (THD). Although the THD of the input voltage is relatively high in both methods, with the proposed method showing a THD of 38.99% and the conventional method at 39.07%, this is primarily due to the DC-AC conversion process in the inverter and the rapid changes in irradiance conditions. However, both methods maintain very low THD in phase current, 0.04%, indicating nearly ideal current quality with negligible harmonic distortion.

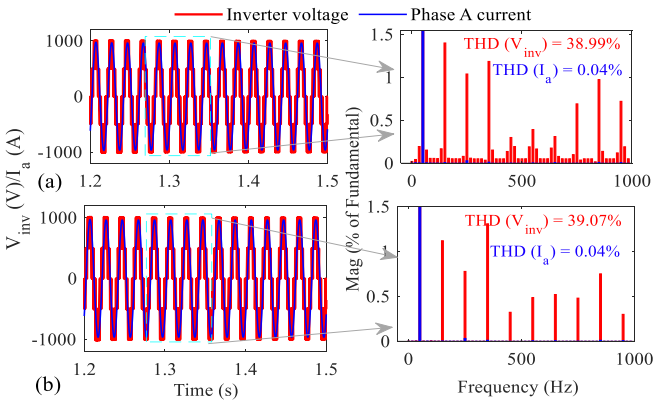

Fig. 19. Comparison of output voltage waveform, phase current, and their THD under normal operating conditions: (a) the proposed method and (b) the conventional method.

The proposed method maintains higher stability in voltage and phase current, with fewer fluctuations than the conventional method, resulting in better system performance. Despite the high harmonic distortion in the input voltage, the proposed method still maintains stable reactive power and better energy quality. In contrast, the conventional method shows greater fluctuations in voltage and current waveforms, leading to higher THD in the input voltage, yet it keeps

reactive power at a low level, indicating reasonable performance under varying light conditions.

4.2. Case Study 2

Considering Grid Fault Condition: LLLG is a common electrical fault that frequently occurs in industrial environments, particularly in renewable energy systems that utilize power electronics, such as inverters and DC-AC converters. When this fault occurs, excessive current can flow, causing significant fluctuations in the system's voltage and current parameters, and posing a risk of damage to semiconductor devices due to their fast response times. Therefore, managing and stabilizing voltage and current during the fault event is crucial to protect the system [34]. In this simulation, an LLLG fault at the PCC bus with a duration of 0.1 seconds occurs at 0.4 seconds, while the irradiance is maintained at 1000 W/m^2 throughout the simulation period, as shown in Fig. 20. This fault has a noticeable impact on the operational parameters of the PV arrays.

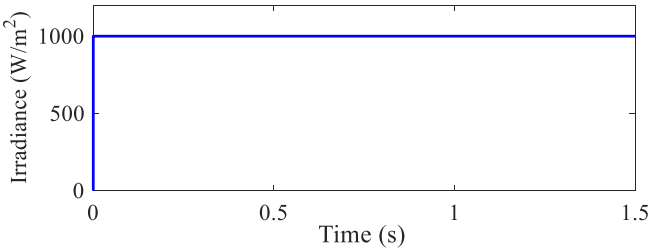

Fig. 20. The solar irradiance pattern applied to PV arrays.

Specifically, as shown in Fig. 21a, the voltage of the PV arrays both increased sharply during the LLLG fault. Within 0.4 to 0.5 seconds, the conventional method caused the voltage to increase from about 650 to 780 V, while the proposed method increased from 690 to 780 V. After the fault was cleared within about 0.5 seconds, the voltage began to recover and stabilize back to its original value of about 650 V for the conventional method and 690 V for the proposed method. Regarding the current, as shown in Fig. 21b, the current of both PVs decreased significantly during the fault. The current almost dropped to 0 A at the time of the fault, indicating an interruption in the power supply from the PV arrays due to the three-phase fault. After the fault is cleared, Fig. 21b shows that the current recovers and increases again to approximately 2000 A for the conventional method and 2300 A for the proposed method, indicating a gradual return to stability.

Regarding power, Fig. 21c shows that the output power from the PV arrays drops sharply during the LLLG fault. Observing from this figure, the power drops from a high value of about 14×10^5 W to nearly 0 MW for the proposed method and from 15×10^5 W to nearly 0 MW for the conventional method, indicating that both PV arrays are unable to supply power during the fault. However, immediately after the fault is cleared, the power recovers rapidly and stabilizes to its initial level, demonstrating the system's ability to quickly return to normal operation. Thus, although there is a significant drop in voltage, current, and power during the LLLG fault, the system recovers rapidly and maintains stability after the fault is cleared.

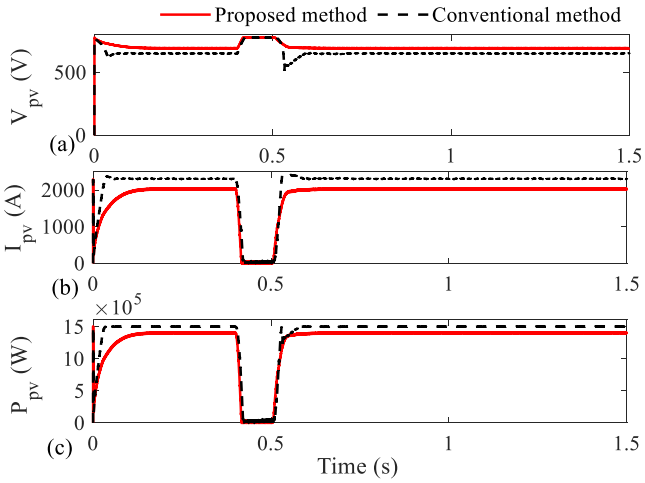

Fig. 21. PV panel parameters: (a) the voltage, (b) the current, and (c) the active power.

The DC voltage suddenly increases at 0.4 seconds, and the conventional method causes it to rise from 1000 to 2071.780 V before dropping back to 1000 V once the fault is cleared, with a settling time of t_{set} = 0.713 seconds. In contrast, the proposed method causes the voltage to rise from 1000 to 1357.660 V before returning to 1000 V when the fault is resolved, with a shorter settling time of t_{set} = 0.539 seconds, demonstrating the proposed method more flexible adjustment and quicker fault recovery, as shown in Fig. 22. The voltage increase for the conventional method is a factor of 2.07 from 1000 to 2071.780 V, while for proposed method, the voltage increase is a factor of 1.36 from 1000 to 1357.66 V.

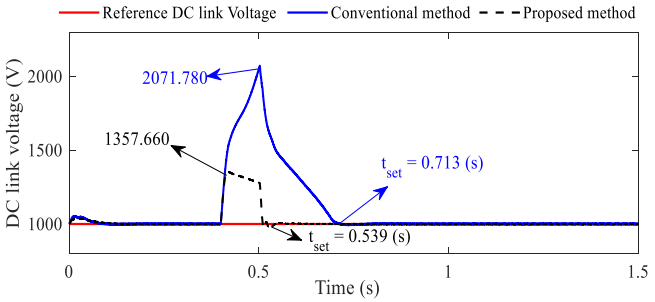

Fig. 22. Dynamic performance of the DC-link voltage under LLLG fault.

The three-phase voltage behavior at the PCC bus during the LLLG fault, using two control methods, the conventional method and the proposed method, is illustrated in Figs. 23a and 23b. The voltage remains constant at 2×10^4 V before the fault. During the fault, the grid voltage drops to zero between 0.4 and 0.5 seconds. The voltage then recovers to its normal level after 0.5 seconds. It is noted that the inverter is off for 0.4 to 0.5 seconds during the fault.

Figs. 24a and 24b present the behavior of the three-phase current at the PCC bus during an LLLG fault under the control of two MPPT methods: the conventional method and the proposed method. In Fig. 24a, the current remains constant at 95 A before the fault occurs, then increases to 560

A during the fault. After the fault is cleared, the current returns to 95 A and stabilizes once the fault is resolved. Similarly, Fig. 24b shows the current at 93 A before the fault, rising to 610 A during the fault, and dropping back to 93 A after the fault is cleared. Once the fault condition ends, the current stabilizes at its normal value of 93 A. Both methods effectively handle the fault, with the proposed method demonstrating slightly better current recovery, suggesting a marginally more efficient response to fault events.

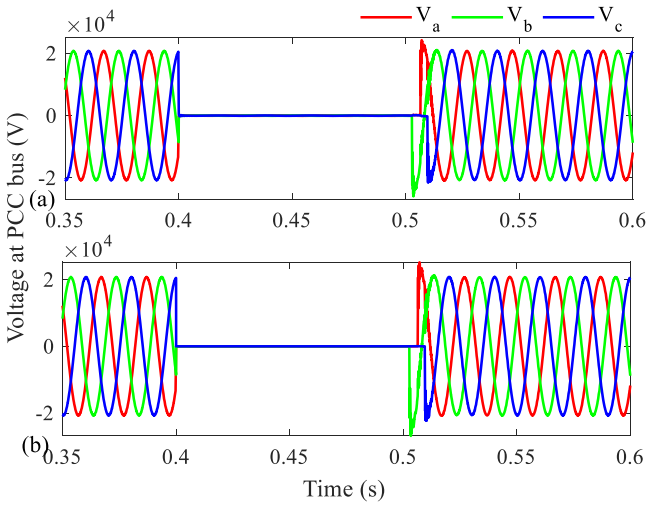

Fig. 23. Dynamic performance of the PCC-Bus voltage under LLLG fault conditions: (a) the proposed method and (b) the conventional method.

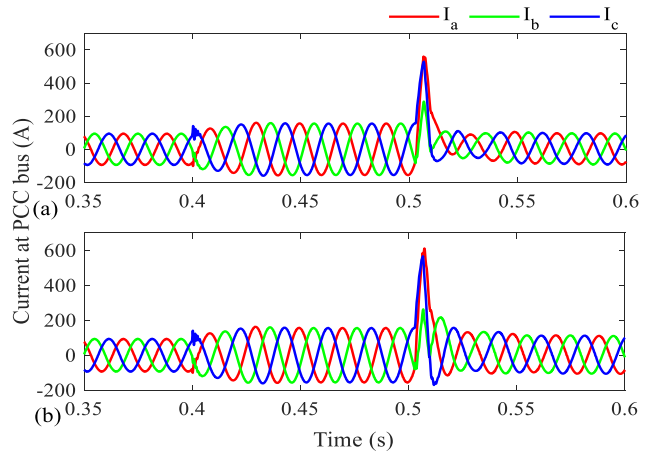

Fig. 24. Dynamic performance of the PCC bus current under LLLG fault: (a) the proposed method and (b) the conventional method.

Based on Figs. 25 and 26, during the LLLG fault, both active power and reactive power for the conventional method and the proposed method experience significant reductions. Specifically, the active power for both methods drops nearly to 0 MW during the fault from 0 to 0.5 seconds. However, the proposed method recovers the active power more quickly, reaching approximately 2.5 MW and stabilizing, whereas the conventional method recovers more slowly, maintaining the power below 2 MW. Regarding reactive power, both methods exhibit substantial fluctuations during the fault, with a peak at the time of the fault. After the fault is cleared, the reactive power of both methods stabilizes at 1.0 MVAr, but the proposed method shows greater reactive power fluctuations, demonstrating its more flexible adjustment and faster recovery compared to the conventional method. In conclusion, the proposed method exhibits faster, more stable power recovery, whereas the conventional method shows slower recovery.

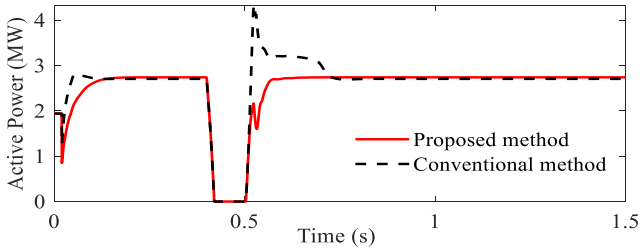

Fig. 25. The active power under LLLG fault.

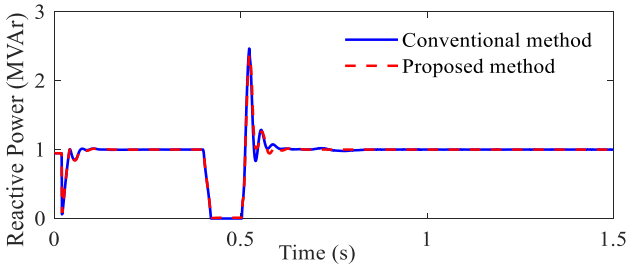

Fig. 26. The reactive power under LLLG fault.

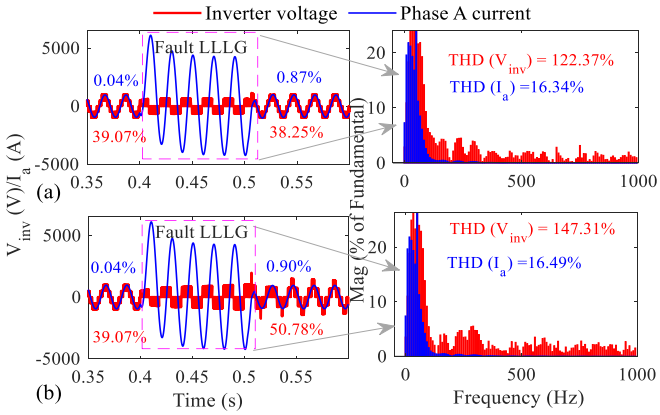

Fig. 27. Comparison of output voltage waveform, phase A current, and their harmonic spectra under LLLG condition: (a) the proposed method and (b) the conventional method.

Table 4. Comparison of inverter voltage and THD (%) of phase A current under conditions of the post-fault, fault-free, and LLLG fault when applying the proposed and the conventional methods

Methods	THD (%)			
	Conditions / Signals	Fault-free	LLLG fault	Post-fault
		(0.35 - 0.4 seconds)	(0.4 - 0.5 seconds)	(0.5 - 0.6 seconds)
Proposed method	V_{inv} (V)	39.07	122.37	38.25
	I_a (A)	0.04	16.34	0.87
Conventional method	V_{inv} (V)	39.07	147.31	50.78
	I_a (A)	0.04	16.49	0.90

Based on Figs. 27a and 27b, and Table 4, during the LLLG fault, both the conventional method and the proposed method exhibit significant fluctuations in voltage and phase current, but the proposed method demonstrates more stable and effective control. Specifically, the conventional method has a voltage THD of 147.31%, which is much higher than the proposed method's 122.37%, indicating that the proposed method maintains a more stable voltage quality during the fault. Although both methods exhibit voltage fluctuations during the fault, the conventional method shows greater distortion, indicating instability in maintaining the output voltage. Regarding phase current, the conventional method has a THD of 50.78%, which is higher than the proposed method at 38.25%, indicating that the conventional method experiences more significant current fluctuations during the fault. The proposed method offers better stability with lower THD, less distortion, and higher current control stability. Overall, the proposed method demonstrates faster recovery and better maintenance of power quality compared to the conventional method during the LLLG fault, thanks to its stability in both voltage and current. The lower THD in both voltage and current for the proposed method demonstrates that it is more effective at minimizing distortion and maintaining system stability under fault conditions.

5. Conclusion

This paper has presented the development and simulation of a grid-connected solar energy conversion system utilizing a three-level NPC inverter and an advanced MPPT controller based on an artificial neural network (ANN) trained with the Levenberg-Marquardt (LM) algorithm. The study evaluated the system's performance in terms of stability, power quality, and fault resilience through a comparative analysis with a conventional dynamic-step-size P&O method. Based on the obtained simulation results, the following conclusions are drawn:

The proposed ANN-LM control strategy significantly improves the DC-link voltage stability under varying irradiance conditions. The quantitative analysis shows that the proposed method reduces the total percentage overshoot to 1.292%, compared to 1.496% for the conventional method. This result indicates that the neural network's nonlinear mapping capability enables more precise tracking of the maximum power point with minimal oscillation, thereby reducing energy losses and mechanical stress on system components compared to traditional gradient-based algorithms.

The simulation of the system under a three-phase-to-ground (LLLG) fault scenario demonstrates the superior dynamic response of the proposed controller. The system utilizing the ANN-LM algorithm achieves a voltage recovery settling time of 0.539 seconds, which is markedly faster than the 0.713 seconds required by the conventional method. Additionally, the voltage surge during the fault is limited to 1.36 times the nominal value with the proposed method, versus 2.07 times with the traditional approach. This rapid recovery is attributed to the predictive nature of the trained neural network, which can instantly estimate the optimal duty cycle, even during severe voltage dips, unlike the reactive adjustments of the P&O method.

The proposed method maintains better power quality during fault conditions, as evidenced by the total harmonic distortion (THD) analysis. During the LLLG fault, the THD of the inverter voltage for the proposed method is 122.37%, significantly lower than the 147.31% recorded for the conventional method; similarly, the phase current THD is reduced to 38.25% compared to 50.78%. This peculiarity suggests that the ANN's robust control of the DC-link voltage effectively mitigates the propagation of harmonic distortions through the inverter during transient states, ensuring safer grid integration.

The application of the Levenberg-Marquardt algorithm for training the neural network resulted in a high correlation coefficient equal to 0.931 across training, validation, and testing phases. This quantitative indicator confirms the MPPT model's precision. The essence of this result lies in the LM algorithm's ability to combine the speed of the Gauss-Newton method with the stability of the steepest descent method, preventing the network from getting trapped in local minima and ensuring reliable performance across diverse operating conditions.

Acknowledgements

The authors would like to thank the managers and the members of the "*International Journal of Smart Grid*" for their valuable remarks and suggestions.

Author Contributions

Le Van Dai was involved in conceptualization, investigation, methodology, software, supervision, writing-original draft, writing -review and editing, formal analysis, and resources. Huynh Hoang Bao Nghia was the methodology, investigation, formal analysis, software, and writing-original draft. All authors have read and agreed to the published version of the manuscript.

Conflict of Interest

The authors declared no potential conflicts of interest with respect to the research, authorship, and/or publication of this article.

Nomenclature

ANN	Artificial Neural Networks
LM	Levenberg-Marquardt
PV	Photovoltaic
LLLG	Three-Phase Ground Faults
MPP	Maximum Power Point
MPPT	Maximum Power Point Tracking
P&O	Perturb and Observe
PLL	Phase-Locked Loop
DC	Direct current
AC	Alternating current
THD	Total Harmonic Distortion
POT	Percentage Overshoot Total
NPC	Neutral Point Clamped

Appendix

Appendix 1. Element parameters.

Manufacture	Symbols	Values
➢ *Three-phase Transformer* (*Yg/Dlta1*)		
Nominal power and frequency	P_n	2.25 MVA
	f_n	50 Hz
Winding 1 parameters	V_1	25e3 V
	R_1	0.001 pu
	L_1	0.03 pu
Winding 2 parameters	V_2	500 V
	R_2	0.001 pu
	L_2	0.03 pu
Magnetization resistance	R_m	200
Magnetization inductance	L_m	200
➢ *Three-phase Transformer* (*Yg/Dlta1*)		
Nominal power and frequency	P_n	47 MVA
	f_n	50 Hz
Winding 1 parameters	V_1	120 kV
	R_1	0.08/30 pu
	L_1	0.08 pu
Winding 2 parameters	V_2	25 kV
	R_2	0.08/30 pu
	L_2	0.08 pu
Magnetization resistance	R_m	500 pu
Magnetization inductance	L_m	500 pu
➢ *Boost Converter*		
Device on-state resistance	R_{db}	$1\times10^{-3}\,\Omega$
Snubber resistance	R_{sb}	$1\times10^{-6}\,\Omega$
➢ *Three-Level NPC Converter*		
Device on-state resistance	R_{on}	$0.5\times10^{-4}\,\Omega$
Snubber resistance	R_{sn}	$1\times10^{-6}\,\Omega$
➢ *Series RL Branch*		
Resistance	R_{sb}	$1\times10^{-3}\,\Omega$
Inductance	L_{sb}	1×10^{-3} H
➢ *Three-Phase Series RL Branch*		
Resistance	R_p	1e-3 Ω
Inductance	L_p	44.2×10^{-6} H
➢ *Invert Control* (*Control system for a* 2 *MW,* 1*MVAr,* 25 *kV, Grid-Connected Inverter*)		
Power	P_n	2.25 MVA
Frequency	f	50 Hz
Primary voltage	V_p	25 kV
Secondary voltage	V_s	500 V
DC voltage	V_{dc}	1.0 kV
Feedforward Values	R_{ff}	0.004 pu
	L_{ff}	0.21 pu
➢ *MPPT Controller*		
Duty cycle initial value	D	0.35
D limits [Upper, Lower]	Upper	0.8
	Lower	0.3
Increment value for the P and O algorithm		60×10^{-6}

Measurement filter cutoff frequency		1000 Hz
➢ *Distributed Parameters* (8 *km*, 2 *km*, 6 *km*, 50 *Hz*)		
Resistance pu length (Ω/km) [NxN matrix]	NxN	0.1153
	matrix	0.413
Inductance pu length (H/km) [NxN matrix]	NxN	1.05×10^{-3}
	matrix	3.32×10^{-3}
Capacitance pu length (F/km) [NxN matrix]	NxN	11.33×10^{-9}
	matrix	5.01×10^{-9}
➢ *Grounding Transformer*		
Nominal power and frequency	P_n	3e6 VA
	f_n	50 Hz
Nominal voltage (Vrms)	V	25 kV
Zero-sequence resistance and reactance	R_0	0.25 Ω
	X_0	7.5 Ω
Magnetization branch	R_0	1.0417×10^5 Ω
	X_0	1.0417×10^5 Ω

References

[1] Z. Reguieg, I. Bouyakoub, F. Mehedi, and F. Bouhadji, "Optimizing Power Quality: Simulation of UPQC Integrated PV with Comprehensive Reliability and Performance Analysis," International Journal of Smart Grid-ijSmartGrid, vol. 8, no. 1, pp. 46-52, 2024, doi: 10.20508/ijsmartgrid.v8i1.333.g338.

[2] V. T. K. Nhi, B. T. Quy, H. H. B. Nghia, and L. V. Dai, "A Robust Hybrid Control Strategy for Enhancing Torque Stability and Performance in PMSM Drives," Electrical Engineering & Electromechanics, no. 6, pp. 64-74, 2025, doi: 10.20998/2074-272X.2025.6.09.

[3] M. Taghavi, H.-J. Yoon, J.-U. Choi, and C.-J. Lee, "Innovative structure of a liquefied natural gas (LNG) process by mixed fluid cascade using solar renewable energy, photovoltaic panels (PV), and absorption refrigeration system," in computer aided chemical engineering, vol. 53: Elsevier, 2024, pp. 2071-2076.

[4] M. Taghavi, H. Salarian, and B. Ghorbani, "Thermodynamic and exergy evaluation of a novel integrated hydrogen liquefaction structure using liquid air cold energy recovery, solid oxide fuel cell and photovoltaic panels," Journal of Cleaner Production, vol. 320, p. 128821, 2021, doi: 10.1016/j.jclepro.2021.128821.

[5] N. V. T. Kieu, N. H. H. Bao, and T. Q. Bach, "A Model Advanced Predictive Current Control Strategy for PMSM Drives with Torque Ripple and Current Harmonic Reduction," Journal of Robotics and Control (JRC), vol. 6, no. 5, pp. 2444-2456, 2025, doi: 10.18196/jrc.v6i5.26908.

[6] B. Ghorbani, G. Salehi, A. Ebrahimi, and M. Taghavi, "Energy, exergy and pinch analyses of a novel energy storage structure using post-combustion CO2 separation unit, dual pressure Linde-Hampson liquefaction system, two-stage organic Rankine cycle and geothermal energy," Energy, vol. 233, p. 121051, 2021, doi: 10.1016/j.energy.2021.121051.

[7] C. N. Dien and H. H. B. Nghia, "Optimizing Permanent Magnet Synchronous Motor Performance Considering Both Maximum Torque Per Ampere and Field Weakening," International Journal of Intelligent Engineering & Systems, vol. 18, no. 1, 2025, doi: 10.22266/ijies2025.0229.81.

[8] Y. Duan, Y. Zhao, and J. Hu, "An initialization-free distributed algorithm for dynamic economic dispatch problems in microgrid: Modeling, optimization and analysis," Sustainable Energy, Grids and Networks, vol. 34, p. 101004, 2023, doi: 10.1016/j.segan.2023.101004.

[9] V. D. Le, "Development of converter configuration and corresponding control strategy for wind turbines using permanent magnet synchronous generator: A Case study," Journal of Energy Systems, vol. 6, no. 4, pp. 484-502, 2022, doi: 10.30521/jes.1025810.

[10] T. T. Nguyen, T. D. Pham, L. C. Kien, and L. Van Dai, "Improved coyote optimization algorithm for optimally installing solar photovoltaic distribution generation units in radial distribution power systems," Complexity, vol. 2020, no. 1, p. 1603802, 2020, doi: 10.1155/2020/1603802.

[11] H. M. H. Farh, A. Fathy, A. A. Al-Shamma'a, S. Mekhilef, and A. M. Al-Shaalan, "Global research trends on photovoltaic maximum power extraction: Systematic and scientometric analysis," Sustainable Energy Technologies and Assessments, vol. 61, p. 103585, 2024, doi: 10.1016/j.seta.2023.103585.

[12] K. Ullah, M. Ishaq, F. Tchier, H. Ahmad, and Z. Ahmad, "Fuzzy-based maximum power point tracking (MPPT) control system for photovoltaic power generation system," Results in Engineering, vol. 20, p. 101466, 2023, doi: 10.1016/j.rineng.2023.101466.

[13] T. Bahi and A. Lakhdara, "Analysis of Genetic and Cuckoo Search Algorithms for MPPT in Partial Shaded," International Journal of Smart Grid-ijSmartGrid, vol. 8, no. 1, pp. 35-40, 2024, doi: 10.20508/ijsmartgrid.v8i1.329.g330.

[14] L. Van Dai, "A novel protection method to enhance the grid-connected capability of DFIG based on wind turbines," IETE Journal of Research, vol. 70, no. 2, pp. 2047-2063, 2024, doi: 10.1080/03772063.2022.2163925.

[15] B. M. Bellah, B. Tahar, and B. Adel, "Adaptive hybrid MPPT using artificial intelligence for an autonomous PV system," International Journal of Smart Grid-ijSmartGrid, vol. 8, no. 1, pp. 27-34, 2024, doi: 10.20508/ijsmartgrid.v8i1.328.g331.

[16] M. H. Zafar, N. M. Khan, A. F. Mirza, and M. Mansoor, "Bio-inspired optimization algorithms based maximum power point tracking technique for photovoltaic systems under partial shading and complex

partial shading conditions," Journal of Cleaner Production, vol. 309, p. 127279, 2021, doi: https://doi.org/10.1016/j.jclepro.2021.127279.

[17] M. Uoya and H. Koizumi, "A calculation method of photovoltaic array's operating point for MPPT evaluation based on one-dimensional Newton–Raphson method," IEEE Transactions on Industry Applications, vol. 51, no. 1, pp. 567-575, 2014, doi: 10.1109/tia.2014.2326083.

[18] M. A. Kamarposhti, I. Colak, H. Shokouhandeh, C. Iwendi, S. Padmanaban, and S. S. Band, "Optimum operation management of microgrids with cost and environment pollution reduction approach considering uncertainty using multi-objective NSGAII algorithm," IET Renewable Power Generation, vol. 19, no. 1, p. e12579, 2025, doi: 10.1049/rpg2.12579.

[19] F. M. Makahleh, A. Amer, A.A. Manasrah, H. Attar, A.A. Solyman, M.A. Kamarposhti, and P. Thounthong, "Optimal management of energy storage systems for peak shaving in a smart grid," Computers, Materials and Continua, vol. 75, no. 2, pp. 3317-3337, 2023, doi: 10.32604/cmc.2023.035690.

[20] N. D. Hung, "Voltage Stability Improvement of Synchronous Generator by Using AVR Self Turning Based on the Adaptive Fuzzy-PID Controller," International Journal of Intelligent Engineering & Systems, vol. 15, no. 6, 2022, doi: 10.22266/ijies2022.1231.42

[21] M. Ahmadi Kamarposhti, H. Shokouhandeh, Y. Gholami Omali, I. Colak, P. Thounthong, and W. Holderbaum, "Optimal coordination of TCSC and PSS2B controllers in electric power systems using MOPSO multiobjective algorithm," International Transactions on Electrical Energy Systems, vol. 2022, no. 1, p. 5233620, 2022, doi: 10.1155/2022/5233620.

[22] I. A. Joneidi, M. A. Kamarposhti, A. A. Shayegani Akmal, and H. Mohseni, "Leakage current analysis, FFT calculation and electric field distribution under water droplet on polluted silicon rubber insulator," Electrical Engineering, vol. 95, no. 4, pp. 315-323, 2013, doi: 10.1007/s00202-012-0260-8.

[23] M. Killi and S. Samanta, "Modified perturb and observe MPPT algorithm for drift avoidance in photovoltaic systems," IEEE transactions on Industrial Electronics, vol. 62, no. 9, pp. 5549-5559, 2015, doi: 10.1109/tie.2015.2407854.

[24] L. Shang, H. Guo, and W. Zhu, "An improved MPPT control strategy based on incremental conductance algorithm," Protection and Control of Modern Power Systems, vol. 5, no. 2, pp. 1-8, 2020, doi: 10.1186/s41601-020-00161-z.

[25] Y. Xiao, Y. Zhao, Z. Shen, and H. Jiao, "SMGSA algorithm-based MPPT control strategy," Journal of Power Electronics, vol. 24, no. 5, pp. 789-798, 2024, doi: 10.1007/s43236-023-00757-2.

[26] D. Van Hoa, H. H. Bao Nghia, and L. Van Dai, "Optimizing permanent magnet synchronous motor control: a comparative study of MPCC-based techniques," Eastern-European Journal of Enterprise Technologies, vol. 135, no. 2, 2025, doi: 10.15587/1729-4061.2025.331895.

[27] L. Wang, H. Liu, L. V. Dai, and Y. Liu, "Novel method for identifying fault location of mixed lines," Energies, vol. 11, no. 6, p. 1529, 2018, doi: 10.3390/en11061529.

[28] X. Liu and Y. Wang, "Reconfiguration method to extract more power from partially shaded photovoltaic arrays with series-parallel topology," Energies, vol. 12, no. 8, p. 1439, 2019, doi: 10.3390/en12081439.

[29] M. Alkahtani, Z. Wu, C. S. Kuka, M. S. Alahammad, and K. Ni, "A Novel PV array reconfiguration algorithm approach to optimising power generation across non-uniformly aged PV arrays by merely repositioning," J, vol. 3, no. 1, p. 5, 2020, doi: 10.3390/j3010005.

[30] A. Belkaid, S. HADJI, and L. Larbi, "Modified Topology of SEPIC Converter with High Gain Transfer Ratio for PV Applications," International Journal of Smart Grid-ijSmartGrid, vol. 8, no. 4, pp. 199-204, 2024, doi: 10.20508/ijsmartgrid.v8i4.363.g368.

[31] B. Dhouib, M. A. Zdiri, Z. Alaas, and H. Hadj Abdallah, "Fault analysis of a small PV/wind farm hybrid system connected to the grid," Applied Sciences, vol. 13, no. 3, p. 1743, 2023, doi: 10.3390/app13031743.

[32] D. Nishad, A. Tiwari, S. Khalid, S. Gupta, and A. Shukla, "AI-based hybrid power quality control system for electrical railway using single phase PV-UPQC with Lyapunov optimization," Scientific Reports, vol. 15, no. 1, p. 2641, 2025, doi: 10.1038/s41598-025-85393-5.

[33] C. D. Loi, H. H. B. Nghia, V. T. K. Nhi, B. T. Quy, and L. Van Dai, "Advanced Speed and Torque Control for PMSM via Adaptive PID and Higher-Order Sliding Mode," International Journal of Intelligent Engineering & Systems, vol. 18, no. 3, 2025, doi: 10.22266/ijies2025.0430.44.

[34] K. Moloi, N. W. Ndlela, and I. E. Davidson, "Fault classification and localization scheme for power distribution network," Applied Sciences, vol. 12, no. 23, p. 11903, 2022, doi: 10.3390/app122311903.